Cosmological 21cm experiments

Jelic, Vibor

Chapter 5

Applications for the LOFAR-EoR experiment

Based on: *Jelić V., et al., 2008, MNRAS, 389, 3, 1319*
Jelić V., et al., submitted to MNRAS

ABSTRACT

Future high redshift 21-cm experiments will suffer from a high degree of contamination, due both to astrophysical foregrounds and to non-astrophysical and instrumental effects. In order to reliably extract the cosmological signal from the observed data, it is essential to understand very well all data components and their influence on the extracted signal. Here we discuss possible statistical effects of the foregrounds on an extraction of the cosmological 21 cm signal from the simulated data. We show that with the expected LOFAR-EoR sky and receiver noise levels, which amount to $\approx$ 52mK at 150 MHz after 400 hours of total observing time, a simple polynomial fit allows a statistical reconstruction of the signal. We also show that the polynomial fitting will work for maps with realistic yet idealized instrument response, i.e., a response that includes only a uniform uv coverage as a function of frequency and ignores many other uncertainties. Moreover, it is demonstrated that an improper instrumental calibration could give rise to leakages of the polarized to the total signal and possibly mask the desired EoR signal.

5.1 Introduction

Currently, a number of experiments (e.g., LOFAR, MWA and SKA) are being designed to directly measure δT_b of the HI 21-cm hyperfine line and probe the physics of the reionization process by observing the neutral fraction of the IGM as a function of redshift. In this study, we focus on predictions for LOFAR, but our conclusions could be easily applied to the other telescopes.

The LOFAR-EoR key project plans to measure the brightness fluctuations in the frequency range of 115–190 MHz, corresponding to redshift range 6–11.5 with spectral resolution of $\approx$ 1 MHz and angular resolution of about $\approx$ 4 arcmin. However, the project

relies on a detailed understanding of astrophysical and non-astrophysical contaminations that can contaminate the EoR signal: the Galactic and extragalactic foregrounds, ionosphere, instrumental effects and systematics. In order to study these components and their influence on the detection of the EoR signal, a LOFAR-EoR simulation pipeline is being developed by the LOFAR-EoR team. The pipeline consists of the three main modules: the EoR signal (based on simulations described in Thomas & Zaroubi, 2008; Thomas et al., 2009), the foregrounds (see Ch. 2 & 3) and the instrumental response (described in Labropoulos et al., 2009a).

Over the years, several methods have been explored to filter out the foregrounds. Most of the methods rely on the relative smoothness in the frequency of the foregrounds, with respect to the signal (e.g. Shaver et al., 1999; Di Matteo et al., 2002; Zaldarriaga et al., 2004; Morales et al., 2006; Wang et al., 2006; Gleser et al., 2008).

Santos et al. (2005) have studied the foregrounds for the EoR experiment and their influence on the measurement of the 21-cm signal. In their multi-frequency analysis of the power spectra, they considered four types of foregrounds: Galactic diffuse synchrotron emission; Galactic free-free emission; extragalactic free-free emission; and extragalactic point sources. They showed that foregrounds cleaning is aided by the large scale angular correlation, especially of the extragalactic point sources, which facilitates signal extraction to a level suitable for the EoR experiments.

In this chapter we use the LOFAR-EoR pipeline to illustrate that with the expected LOFAR-EoR sky and receiver noise levels, a simple polynomial fit allows a statistical reconstruction of the signal. Moreover, we also show the need for excellent calibration of the instrument in order to reliably detect the EoR signal.

Recently, a study by Gleser et al. (2008) has been conducted along lines similar to parts of the current work. The authors test a certain signal extraction algorithm on simulated foregrounds maps in which they take most of the relevant foregrounds into account. However, there are many important differences between the two works. First, in the Gleser et al. (2008) study the assumption for the noise level in the LOFAR-EoR project, as well as the other experiments, is at least an order of magnitude too low. They assume 1 and 5 mK noise models whereas in reality the noise for the LOFAR-EoR experiment is about 50 mK. In contrast to them, we introduce the LOFAR instrumental response and noise in a realistic manner.

The chapter is organized as follows. Section 5.2 & 5.3 give brief overviews of the cosmological 21 cm and instrumental response simulations. Section 5.4 discusses a method to extract the EoR signal from the foregrounds. We illustrate the need for a good polarization calibration in Sec. 5.5. The chapter finishes with a summary and conclusions (Sec. 5.6).

5.2 The Cosmological 21-cm signal

In radio astronomy, where the Rayleigh-Jeans law is applicable, the radiation intensity, $I(\nu)$ is expressed in terms of the brightness temperature T_b, such that:

$$I(\nu) = \frac{2\nu^2}{c^2} k T_b, \tag{5.1}$$

where ν is the frequency, c is the speed of light and k is Boltzmann's constant. The predicted differential brightness temperature deviation of the cosmological 21-cm signal from the cosmic microwave background radiation is given by (Field, 1958, 1959; Ciardi & Madau, 2003b):

$$\delta T_{\rm b} = 26 \text{ mK } x_{\rm HI}(1+\delta)\left(1-\frac{T_{\rm CMB}}{T_{\rm s}}\right)\left(\frac{\Omega_{\rm b}h^2}{0.02}\right)\left[\left(\frac{1+z}{10}\right)\left(\frac{0.3}{\Omega_{\rm m}}\right)\right]^{1/2}. \tag{5.2}$$

Here $T_{\rm s}$ is the spin temperature, $x_{\rm HI}$ is the neutral hydrogen fraction, δ is the matter density contrast, $\Omega_{\rm m}$ and $\Omega_{\rm b}$ are the mass and baryon density in units of the critical density and $h = H_0/100$. Throughout we assume ΛCDM-cosmology with WMAP3 parameters (Spergel et al., 2007): $h = 0.73$, $\Omega_{\rm b} = 0.0418$, $\Omega_{\rm m} = 0.238$ and $\Omega_\Lambda = 0.762$.

In his seminal papers, Field (1958, 1959) used the quasi-static approximation to calculate the spin temperature, T_s, as a weighted average of the CMB, kinetic and colour temperature (Wouthuysen, 1952; Field, 1958):

$$T_s = \frac{T_{CMB} + y_{kin}T_{kin} + y_\alpha T_\alpha}{1 + y_{kin} + y_\alpha}, \tag{5.3}$$

where T_{CMB} is the CMB temperature and y_{kin} and y_α are the kinetic and Lyman-α coupling terms, respectively. We have assumed that the color temperature, T_α, is equal to T_{kin}. The kinetic coupling term increases with the kinetic temperature, whereas the y_α coupling term is due to the Lyman-α pumping, known also as the Wouthuysen-Field effect (Wouthuysen, 1952; Field, 1958). The two coupling terms are dominant under different conditions and in principle could be used to distinguish between ionization sources, e.g., between first stars, for which Lyman-α pumping is dominant, vs. first mini-quasars for which X-ray photons and therefore heating is dominant (see e.g., Nusser, 2005; Kuhlen et al., 2006; Zaroubi et al., 2007; Thomas & Zaroubi, 2008).

The cosmological 21 cm maps (δT_b) used in this study are based on a dark-matter-only N-body simulation, i.e., the density as a function of right ascension, declination, and redshift (Thomas & Zaroubi, 2008, for more details see). Although T_s is calculated according to Eq. 5.3, we assume that $T_s \gg T_{CMB}$. The reason for this assumption is that towards the redshifts of interest for the experiment ($z = 6 - 12$), the abundance of Lyα photons in the Universe is sufficient to couple T_s to T_k which is obviously much greater than T_{CMB} (Ciardi & Madau, 2003b). Hence from Eq. 5.2, T_b follows the cosmological density and x_{HI}. We further assume that along each sight-line the neutral fraction follows the function $1/\left(1+\exp(z - z_{reion})\right)$, where z_{reion} for each pixel (or line of sight) is set to $8.5 \pm \delta_{z=10}$ and where $\delta_{z=10}$ is the density contrast at redshift 10. We used this approach to randomize the reionization histories along different lines of sight while preserving the spatial correlations of the cosmological signals. In principle, this randomization could be drawn out of a Gaussian distribution function. Redshift 10 here is an arbitrary choice. z_{reion} along each line of sight varies in accordance with the cosmological density along that line-of-sight at $z = 10$ and has a variance of unity centered at 8.5. Fig. 5.1 shows an example of the EoR data cube produced by this simulation.

Recently, the described simulation is developed further and implemented in the BEARS algorithm (Thomas et al., 2009). BEARS is a fast algorithm to simulate the underlying cosmological 21 cm signal from the EoR. It uses an N-body/SPH simulation in conjunction

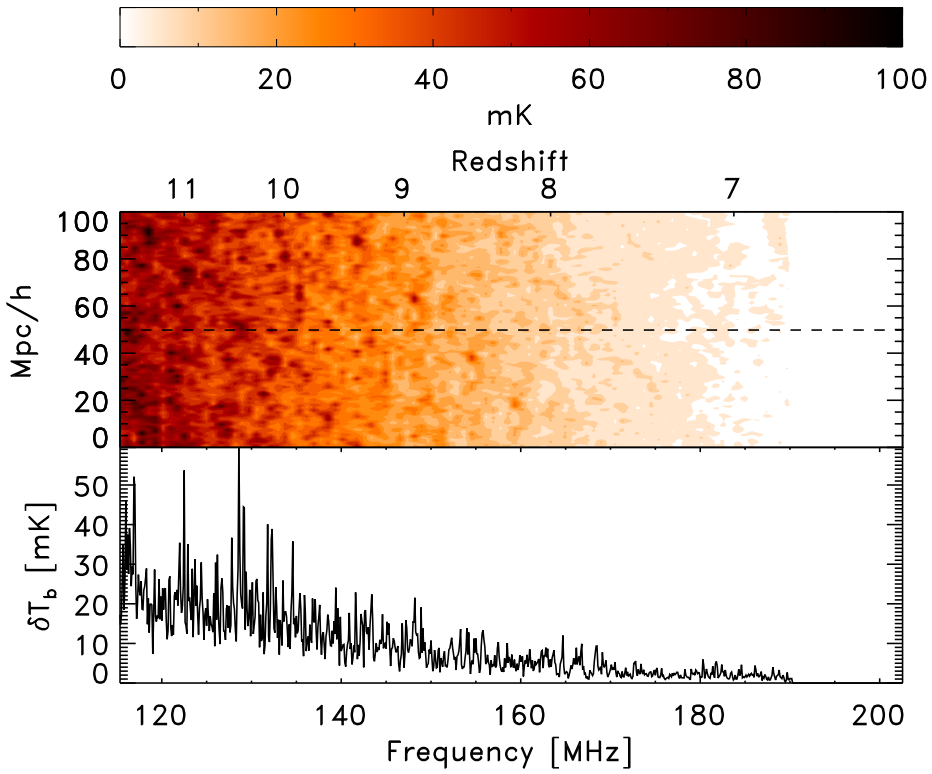

Figure 5.1: Simulated EoR signal assuming an exponential form for the reionization history as decribed in the text and $T_s \gg T_{CMB}$. The simulation box is 100 Mpc h^{-1} (comoving) a side. The upper panel shows the differential brightness temperature in a slice along the redshift/frequency direction and another spatial direction. The lower panel shows the brightness temperature as a function of redshift/frequency along a certain sight line (the dashed line in the upper panel). The resolution along the frequency direction is 10 kHz.

with a 1-D radiative transfer code under the assumption of spherical symmetry of the ionized bubbles. The basic steps of the algorithm are as follows: first, a catalogue of 1D ionization profiles of all atomic hydrogen and helium species and the temperature profile that surround the source is calculated for different types of ionizing sources with varying masses, luminosities at different redshifts. Subsequently, photon rates emanating from dark matter haloes, identified in the N-body simulation, are calculated semi–analytically. Finally, given the spectrum, luminosity and the density around the source, a spherical ionization bubble is embedded around the source, whose radial profile is selected from the catalogue as generated above. For more details we refer to Thomas et al. (2009).

5.3 Instrumental response

In this section we give a basic overview of the simulations of LOFAR antenna response and show how the foreground maps are seen by LOFAR. More detailed discussion on the LOFAR response and data model for the LOFAR-EoR experiment will appear in Labropoulos et al. (2009a, in prep.). For the LOFAR-EoR experiment we plan to use the LOFAR core, which will consist of approximately 25 stations. However, in this chapter we set the number of LOFAR core stations to 24. Each station is further split into two substations which are separated by a few tens of metres (see Fig. 5.2). Each substation consists of 24 tiles, with each tile having 4×4 crossed dipoles. For our goals we assume that each of the forty-eight substations is a circular array with a radius of thirty-five metres. The stations are distributed in a randomized spiral layout and span a baseline coverage from 40 to 2000 metres. The total effective collecting area for the LOFAR-EoR experiment is ~ 0.07 km^2 at 150 MHz. The instantaneous bandwidth of the LOFAR telescope is 32 MHz and the aim for the LOFAR-EoR experiment is to observe in the frequency range between 115–180 MHz, which is twice the instantaneous bandwidth. To overcome this, multiplexing in time has to be used. For the purpose of this chapter we ignore this complication and assume 400 hours of integration time for the hole frequency range.

In order to compute the true underlying visibilities, we make some simplifying assumptions. We assume that the narrow bandwidth condition holds and that the image plane effects have been calibrated to a satisfactory level. This includes station complex gain calibration, a stable primary beam, and adequate compensation for the ionospheric effects, such that the ionospheric phase introduced during the propagation of electromagnetic waves in the ionosphere and the ionospheric Faraday rotation are corrected for. For an interferometer, the measured spatial correlation of the electric fields between two antennae is called 'visibility' and is approximately given by Taylor et al. (1999):

$$V_f(u,v) = \int A(l,m) I_f(l,m) \mathrm{e}^{i(ul+vm)} \mathrm{d}l\mathrm{d}m$$

where A is the primary beam, I_f is the intensity map corresponding to frequency f, (u,v) are the coordinates, as seen from the source, of the tracks followed by an interferometer as the Earth rotates, and (l,m) are the direction cosines.

We further treat each pixel of the map as a point source with the intensity corresponding to intensity of the pixel. Note that the equation above takes into account the

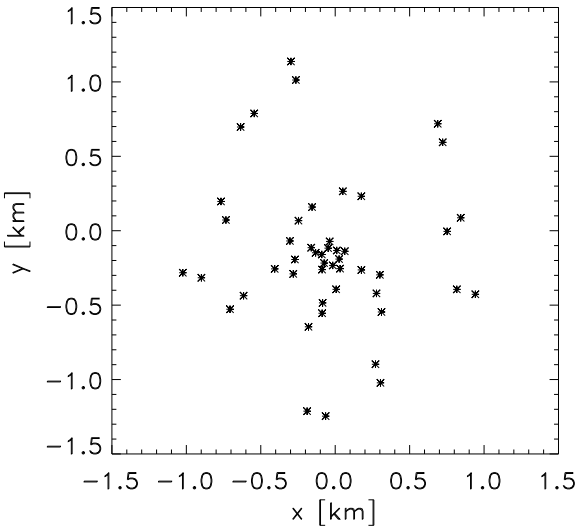

Figure 5.2: Position of 48 substations (24 stations) of the LOFAR core used for simulations of instrumental effects. Note that each substation consists of 24 tiles, with each tile having 4×4 crossed dipoles.

sky curvature. The visibilities are sampled for all substation pairs and also at different pair positions, as the Earth rotates.

We calculate the Fourier transform of the foreground model for each frequency in the above range. For every baseline and frequency, the uv tracks sample different scales of the Fourier transform of the sky at that frequency. Thus, the sampling function S becomes

$$S(u,v) = \sum_k \delta\left(u - u_k\right)\delta\left(v - v_k\right), \tag{5.4}$$

where the summation is carried over all the pixels k.

We compute those tracks for each interferometer pair for 4 hours of synthesis with an averaging interval of 100 s and we then grid them on a regular grid in the uv plane. The maximum baseline assumed for the LOFAR core is 2 km and the station diameter is 35 m, the number of independent elements in the uv plane is $\approx 60^2$. If the uv plane is oversampled by a factor of four, this yields 256^2 pixels [1] in the uv plane of ≈ 60 m^2 in size. After counting how many track points fall within each grid cell, we end up with a matrix representing the naturally weighted sampling function in the uv plane. By multiplying this sampling matrix with the Fourier transform of our model sky we get the visibilities on that grid with appropriate weights. This procedure is done for each baseline pair.

$$V_f\left(u,v\right) = S \cdot \mathcal{F}I \tag{5.5}$$

[1] This is the closest power of two to match the number of sampled elements. By doing this one can benefit from the speed of the FFT.

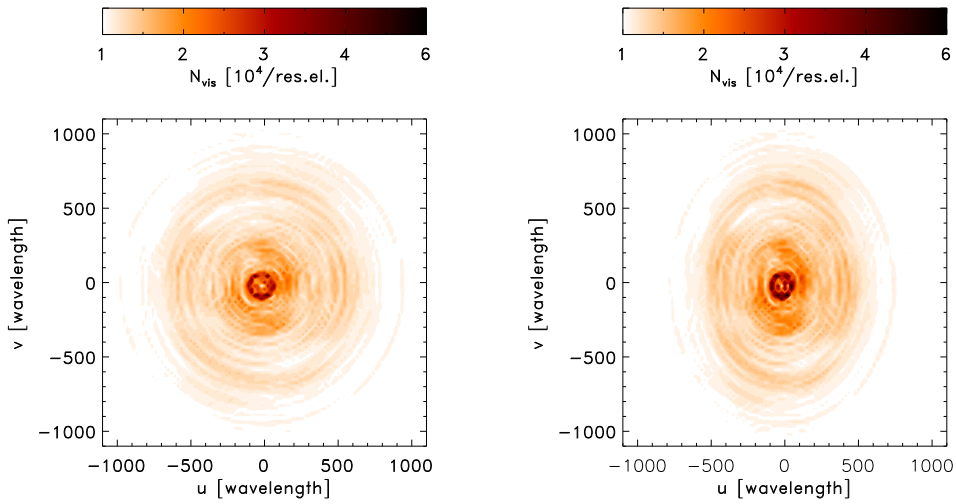

Figure 5.3: The expected LOFAR visibility densities per resolution element at 150 MHz for 400 h of total integration time (100×4 h night^{-1}) with averaging time of 100 s and for observing declinations $\delta = 90°$ (left panel) and $\delta = 52°$ (right panel).

where $\mathcal{F}I$ is the Fourier transform of the input image and S is the sampling function.

The LOFAR visibility densities per resolution element at 150 MHz, for the LOFAR-EoR experiment, are shown in Fig. 5.3. The total integration time is 400 hours (100×4 h night^{-1}) with averaging time of 100 s and observing declinations $\delta = 90°$ (left panel) and $\delta = 52°$ (right panel).

The inverse Fourier transform of the sampled visibilities is called the 'dirty' map. It is actually the sky map convolved with the Fourier transform of the sampling function, which is called the 'dirty' beam or the 'PSF'. This is a simple-minded approach to estimating the sky brightness as it uses linear operations. The approximation of the underlying brightness with the 'dirty' map is not always satisfactory, as side lobes from bright features will obscure fainter ones. In cases of low signal to noise, however – such as during the observation of the redshifted 21-cm transition line of HI – one might choose not to proceed further than this first approximation. To go beyond that we need extra information like the positivity of the intensity and compact support. The discussion of such issues is beyond the scope of this chapter. This incomplete sampling of the uv plane also means that we do not measure the complete power at all scales, due to the holes in the uv coverage and its finite extent.

An example of a 'dirty' map of the diffuse components in the foregrounds is shown in the Fig. 5.4, together with the 'original' simulated foreground map with no interferometric effects and noise. The corresponding total integration time is 400 hours, with an averaging time of 100 s at 150 MHz. Note that the 'dirty' maps are generated without the inclusion of noise.

Recently, the above procedure is developed further and implemented as a parallel algorithm in the CHOP^2 simulation (see Labropoulos et al, *in preparation*). This new

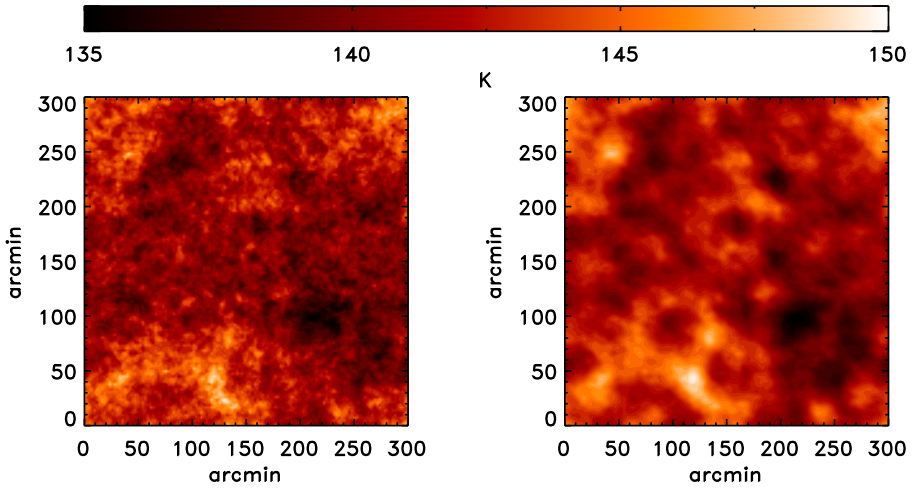

Figure 5.4: Total intensity map of the simulated diffuse components of the foregrounds (left panel; 'original' map with no interferometric effects and noise) and its corresponding 'dirty' map (right panel) after 400 h of total integration time with averaging of 100 s at 150 MHz.

simulation includes all instrumental effects, e.g. primary beam and scaling of the uv coverage with the frequency. An example of a 'dirty' map produced by the CHOP[2] simulation is presented on Fig. 5.5.

Figure 5.5 shows 'dirty' maps of the simulated Galactic synchrotron emission (MODEL B) observed (4hrs of synthesis, 10 sec integration) with the core stations of the LOFAR telescope at 138 MHz. The total and polarized intensity maps are shown on the *first* and the *second panel*, while the polarization angle is presented on the *third panel*. Note that the large scale structures of the emission are missing as the smallest baseline length is approximately 50 m. In order to sample the large structure of the foregrounds at scales between 5 and 10 degrees we need interferometer spacing between 6.5 and 13 meters. Thus the PSF acts as a high-pass spatial filter.

The ultimate sensitivity of a receiving system is determined principally by the system noise. The discussion of the noise properties of a complex receiving system like LOFAR can be lengthy, so we concentrate for our purposes on some basic principles. The theoretical rms noise level in terms of flux density on the final image is given by

$$\sigma_{noise} = \frac{1}{\eta_s} \times \frac{SEFD}{\sqrt{N \times (N-1) \times \Delta\nu \times t_{\rm int}}} \tag{5.6}$$

where η_s is the system efficiency that accounts for electronic, digital losses, N is the number of substations, $\Delta\nu$ is the frequency bandwidth and $t_{\rm int}$ is the total integration time. SEFD is the System Equivalent Flux Density in Jy. The system noise we assume has two contributions. The first comes from the sky and is frequency dependent ($\approx \nu^{-2.55}$) and the second from receivers.

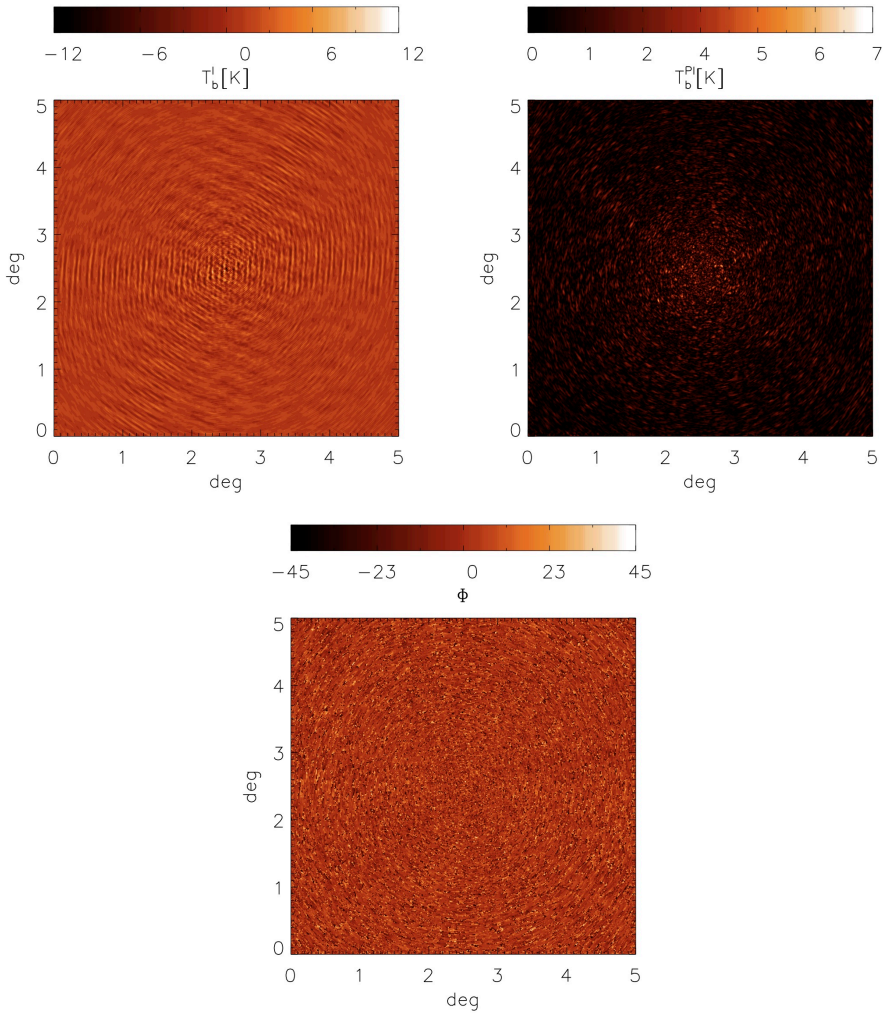

Figure 5.5: 'Dirty' maps of the simulated Galactic synchrotron emission (MODEL B in Ch. 3) observed with the core stations of the LOFAR telescope (4hrs of synthesis, 10 sec integration). The total and polarized intensity maps are shown on the *first* and the *second panel*, while the polarization angle is presented on the *third panel*. The images are simulated at 138 MHz with the CHOP[2] simulation, which implements all instrumental effects.

For the LOFAR core the SEFD will be around 1000 Jy at 150 MHz, depending on the final design. This means that we can reach a sensitivity of 520 mK at 150 MHz with 1 MHz bandwidth in one night of observations. In order to calculate the SEFD we use the following system temperature (T_{sys}) scaling relation as function of frequency (ν): $T_{sys} = 140 + 60(\nu/300\ \mathrm{MHz})^{-2.55}$. Accumulating data from a hundred nights of observations brings the sensitivity down to 52 mK. We further assume that the distribution of noise over the map at one frequency is Gaussian. The noise contribution to each pixel in a map is drawn independently from a Gaussian distribution. The EoR signal is extracted from two different scenarios. The first scenario involves the extraction of the signal from the 'original' maps – simulated maps that are not convolved with the dirty beam – after adding the noise directly to the 'original' maps. In the other scenario, the EoR signal is extracted from 'dirty' maps to which we do not add noise but convolve the 'original' maps of the EoR signal plus the foregrounds with a simplified dirty beam.

As the uv coverage scales linearly with frequency, one has to be careful in using the 'dirty' maps for extraction. This is because a pixel sampled at a given frequency need not be sampled at a later frequency. Since the analysis performed in this chapter involves data across the frequency domain, we need a good uv coverage. If the uv sampling functions are not scaled accordingly, we will introduce additional difficulties arising from the mixing of spatial scales. To overcome spatial scale mixing, one of the strategies in the data analysis is to use only the uv points that are present at all frequencies. In other words one can construct the uv plane mask that only contains the uv points that are sampled at every frequency. This step of course results in substantial data loss.

The uv coverage for the LOFAR-EoR experiment changes in scale by $\sim 40\%$ between the frequency range of observation (115–180 MHz). By choosing only those uv points that are present at all frequencies, $\sim 5\%$ of the total data is lost in the frequency range specified above. Since with decreasing bandwidth of observation the amount of data lost decreases, one of the strategies could be to observe in windows of smaller bandwidth. However the observational strategy of the LOFAR-EoR experiment is not yet finalized and will be discussed in detail in upcoming papers of the project. A detail discussion on the scaling of the uv coverage with frequency and its influence on the number of discarded baselines and the amount of data loss will be discussed in (Labropoulos et al., 2009a, in prep.).

5.4 Detection of the EoR signal from the FG

This section presents the results on the statistical detection of the EoR signal from 'original' and 'dirty' LOFAR-EoR data maps that include the cosmological 21cm signal, diffuse components of the foregrounds and realistic noise. By 'original' maps we mean maps before inversion or in other words maps with no calibration errors or interferometric effects. 'Dirty' maps include only simplified uv coverage effect as an interferometric effect (the uv mask contains only uv points present at each frequency), but neither calibration errors nor other systematics that might influence the data. In both cases the statistical detection of the signal is done on total intensity maps only.

By using only diffuse components of the foregrounds (Galactic diffuse synchrotron and free-free emission and integrated emission from unresolved extragalactic sources) we

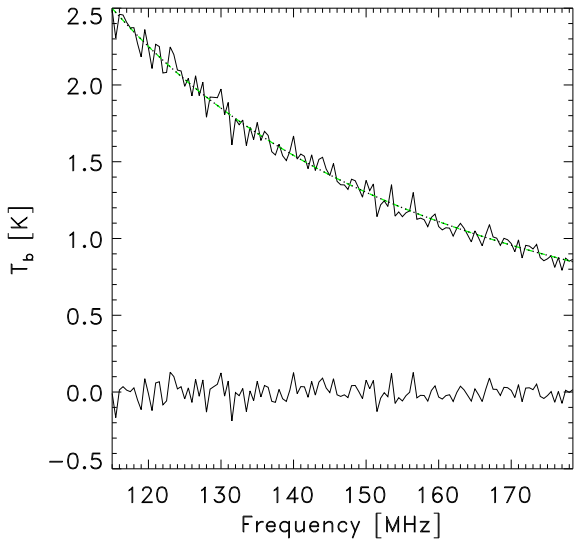

Figure 5.6: One line of sight (one pixel along frequency) of the 'original' LOFAR-EoR data maps (upper solid black line), smooth component of the foregrounds (dotted black line), fitted foregrounds (dashed green line) and residuals (lower solid black line) after taking out the foregrounds. Note that the residuals are the sum of the EoR signal and the noise.

assume that all resolved discrete and extended sources have been successfully removed from the observed maps, without any subtraction residuals. Also note that our analysis is done on total intensity maps only.

The foreground and noise maps are simulated in the frequency range between 115 MHz and 178.5 MHz in steps of 0.5 MHz. The original maps simulated for a $5^\circ \times 5^\circ$ field on a 512^2 grid are re-binned to a 128^2 grid, so that each pixel corresponds to $2.3'$ which is the resolution attained by the core of the LOFAR telescope.

The EoR maps are simulated between the frequencies of 115 MHz and 178.5 MHz in steps of 0.5 MHz, corresponding to redshifts between 11.5 and 6.5.

The mean of the EoR signal, foreground and noise maps at each frequency are set to zero since LOFAR is an interferometric instrument and measures only fluctuations around the mean. The typical variations, σ, over the map at 150 MHz are ~ 5 mK for the EoR signal, ~ 2 K for the foregrounds and ~ 52 mK for noise. Hereafter, these values are considered fiducial values for the EoR signal, foregrounds and noise.

The analysis on the LOFAR-EoR data maps can be done in two ways: firstly along the frequency direction where the foregrounds are assumed to be smooth in contrast to the EoR signal; and secondly in the spatial domain where the EoR signal and some components of the foregrounds are spatially correlated, but the noise is not. In this chapter we will demonstrate statistical detection of the signal by analysis along the frequency direction, taking lines of sight (map pixels) one by one.

Fig. 5.6 shows one line of sight (one pixel along frequency) of the 'original' LOFAR-

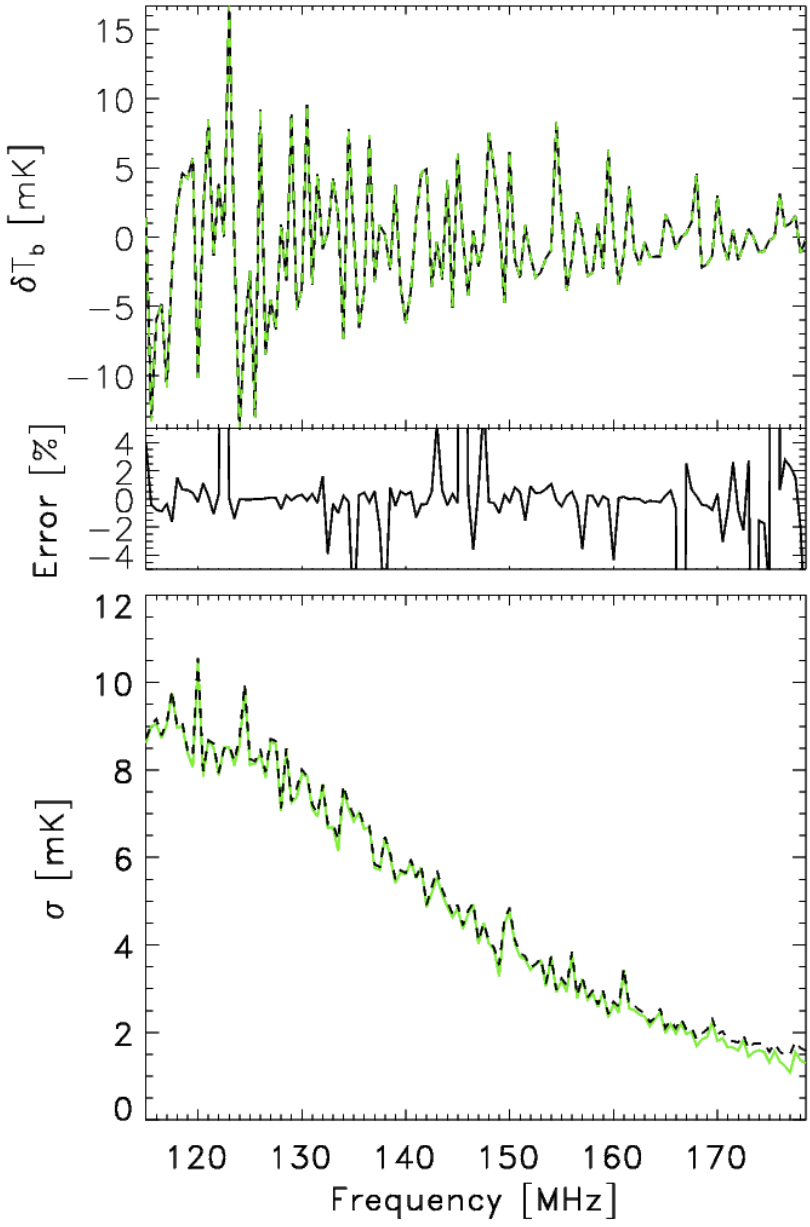

Figure 5.7: Detection of the EoR signal from the simulated foreground maps ('original' maps), without interferometric effects and noise: for a single random line of sight (top panel) and as a standard deviation over all lines of sight (bottom panel). The solid green line represents the original simulated EoR signal, and the dashed black line the extracted EoR signal.

EoR data cube (upper black solid line) without interferometric effects. The first step in the extraction of the EoR signal is to take out the smooth foreground component (dotted black line). It is important to note, however, that the smooth component of the foregrounds is not a simple power law but a superposition of three power laws (Galactic synchrotron and free-free emission and integrated emission from unresolved extragalactic sources) including the fact that one of the power law indices β (Galactic synchrotron emission) changes slightly with frequency.

The simplest method for foreground removal is a polynomial fitting in logarithmic scale ($\log(T_b) - \log(\nu)$). The dashed green line on Fig. 5.6 represents the foregrounds fitted with a 3$^{\rm rd}$ order polynomial in the logarithmic scale.

Fig. 5.7 shows a comparison between the detected and original EoR signal for randomly chosen lines of sight in the case of the fiducial foreground level and without noise for 'original' maps. As one can see, there is an almost exact agreement: this confirms that our approach when applied to noiseless data does not introduce any systematic biases.

After taking out the fitted foregrounds from the 'original' data maps, the residuals should contain only the noise and the EoR signal (lower solid black line on Fig. 5.6). However, the assumption here is that we have fitted well enough such that the residuals between the fitted and the 'real' foregrounds are smaller than the EoR signal. Otherwise the EoR signal could be fitted out if we are over-fitting, or be dominated by the foreground fitting residuals if we are under-fitting the foregrounds.

The extraction of the EoR signal from the residuals along one line of sight is an impossible task, since the level of the noise is order of magnitudes larger than EoR signal and its value is unknown for a certain pixel. However, general statistical properties of the noise (standard deviation as a function of frequency) might be determined from the experiment and be used to statistically detect the EoR signal. By statistical detection we mean determination of the standard deviation of the EoR signal over the entire map as an excess variance over the variance of the noise. The general statistical properties of the noise might be determined in two ways. The first method is based on the difference between measured fluxes of a discrete point source, with well know properties, at two consecutive frequency channels. The second one is based on the difference between the measured flux in total and polarized intensity at the same frequency. However, the accuracy of the both methods need to be tested for the LOFAR-EoR experiment and we leave further discussion on this topic for a forthcoming paper.

Fig. 5.8 shows the standard deviation of residuals as a function of frequency (dotted green line), after taking out the smooth component of the foregrounds, by polynomial fitting in logarithmic scale to each line of sight of the 'original' maps. The most satisfactory result we get with a 3$^{\rm rd}$ order polynomial. The dashed-dotted black line represents the standard deviation of the noise. By subtracting (in quadrature) the $\sigma_{\rm noise}$ from $\sigma_{\rm residuals}$, we get the excess variance ($\sigma_{\rm EoR}$) of the EoR signal. However, in order to determine the error on the detection of the EoR signal, we conducted a Monte-Carlo simulation of the extraction of the signal. We made 1000 independent noise cube realisations and applied the signal extraction algorithm to each. The results of the simulation are shown in Fig. 5.8. The grey shaded zone shows the 2σ detection, whereas the dashed white line shows the mean of the detection. As one can see the mean of the detected EoR signal is in good agreement with the original (solid red line) up to 165 MHz. The disagreement for higher frequencies is due to over-fitting and low EoR signal level. Remember that for

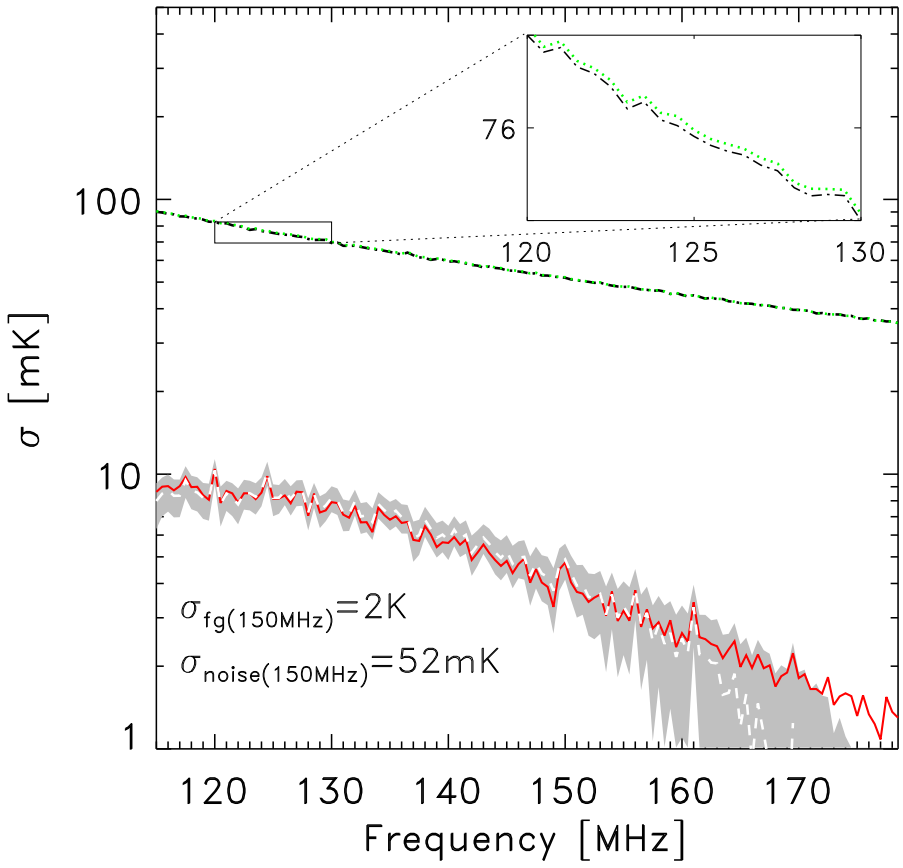

Figure 5.8: Statistical detection of the EoR signal from the 'original' LOFAR-EoR data maps that include diffuse components of the foregrounds and realistic noise ($\sigma_{\rm noise}(150\ {\rm MHz}) = 52$ mK) but without interferometric effects. The dashed-dotted black line represents the standard deviation (σ) of the noise as a function of frequency, the dotted green line the σ of the residuals after taking out the smooth foreground component, and the solid red line the σ of the original EoR signal. The grey shaded zone shows the 2σ detection, whereas the dashed white line shows the mean of the detection. Note that the y-axis is in logarithmic scale.

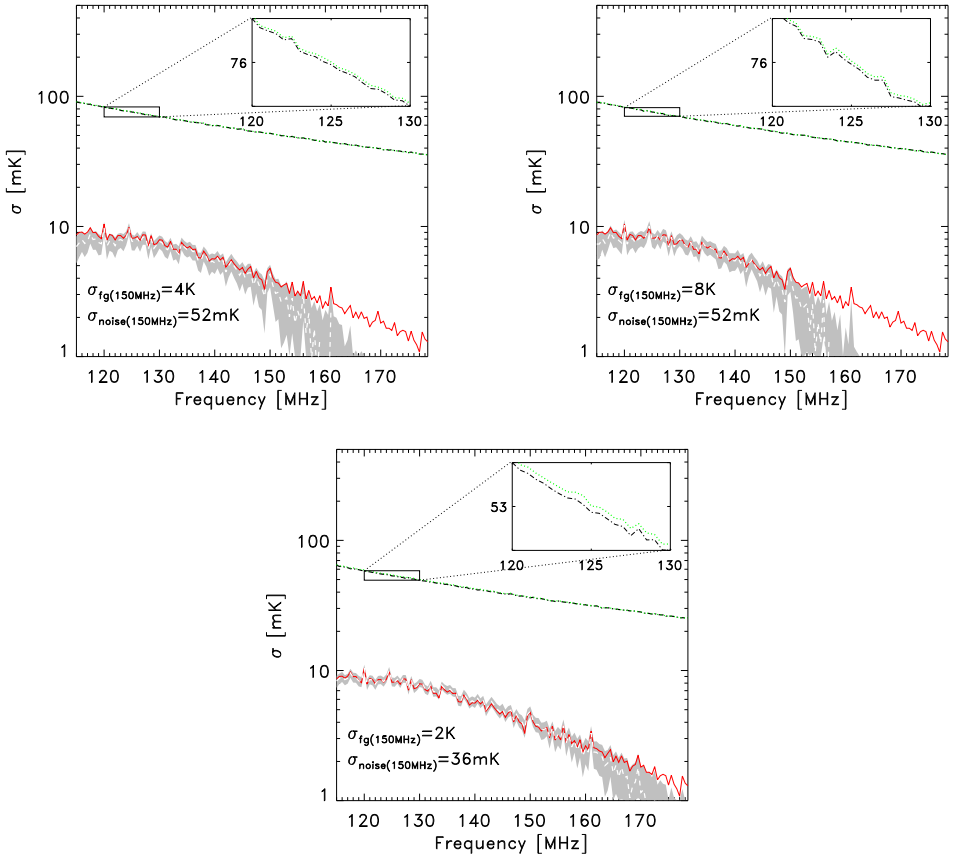

Figure 5.9: Statistical detection of the EoR signal from the 'original' LOFAR-EoR data maps with foreground level two (left panel) and four (middle panel) times bigger than the fiducial foreground level, and with noise level smaller by $\sqrt{2}$ (right panel) than the fiducial noise level, but without interferometric effects. Colours and line coding are the same as in Fig. 5.8. Note that the y-axis is in logarithmic scale.

Table 5.1: Five different sets of values for standard deviation of foregrounds (σ_{fg}[K] at 150 MHz) and of noise (σ_{noise}[mK] at 150 MHz), used for testing the EoR extraction and detection scheme. Note that case (a) represents the fiducial case.

	case (a)	case (b)	case (c)	case (d)	case (e)
σ_{fg}[K]	**2**	4	8	2	2
σ_{noise}[mK]	**52**	52	52	36	0

most of the sightlines our simulated Universe has already been ionized at this frequency, corresponding to $z \approx 7.5$ (see section 5.2).

In order to see the influence of the foreground and noise level on the EoR extraction and detection scheme, we repeated the same analysis on 'original' maps of the four different models. The first model has a foreground level two times bigger than fiducial and the second four times; the third has the fiducial foreground level but smaller noise level by $\sqrt{2}$; and the last one has a normal foreground level and no noise (see Table 5.1). Note that by fiducial foreground level and noise level we mean $\sigma_{fg}(150\text{ MHz}) \sim 2$ K and $\sigma_{\rm noise}(150\text{ MHz}) \sim 52$ mK. The results are shown in Figs. 5.7 & 5.9.

Comparing Figs. 5.8 & 5.9, we see the higher foreground levels decrease the quality of the EoR detection. Lower quality in the EoR detection is due to over-fitting at higher frequencies. However, even for the four times bigger foreground level we are able to detect the EoR signal up to 150 MHz.

Comparing Figs. 5.7, 5.8 & 5.9, we can see that a lower noise level increases the quality of the EoR detection, as expected. Better precision in the EoR detection with lower noise level also confirms that our foreground removal procedure works well.

Finally, in Fig. 5.11, we show the statistical detection of the EoR signal from the 'dirty' foregrounds + EoR signal maps without any noise. Note that the 'dirty' maps are produced with a sampling function (uv mask) that contains only uv points present at each frequency, in order to overcome additional difficulties from the mixing of angular scales in the frequency direction introduced by the linear frequency variation of the uv coverage and incomplete sampling in the frequency direction.

The smooth component of the foregrounds is removed by polynomial fitting to each line of sight. The most satisfactory result we get with a $6^{\rm th}$ order polynomial. A different order of polynomial from the case of the 'original' maps is required due to the angular scale mixing over each map introduced by convolution of the map with a 'dirty' beam.

Fig. 5.10 shows a comparison along the frequency direction of the same pixel from the 'original' (solid line) and 'dirty' (dashed line) foregrounds + signal maps. Note that the foregrounds are still smooth along the frequency direction of the 'dirty' maps, but the shape of the function is slightly different. The difference is due to incomplete uv coverage sampling and its finite extent, determined by the shortest and longest baselines.

The dashed green line in Fig. 5.11 shows the standard deviation, as a function of frequency, of the extracted EoR signal from 'dirty' foregrounds + EoR signal maps. The dashed-dotted black line shows the standard deviation of the 'original' EoR signal maps, while the solid black line shows the standard deviation of the 'dirty' EoR signal maps. The agreement between the standard deviations of the extracted and 'dirty' EoR signals is satisfactory, while their slightly lower levels than the 'original' signal are due to the smoothing effect of the instrumental response.

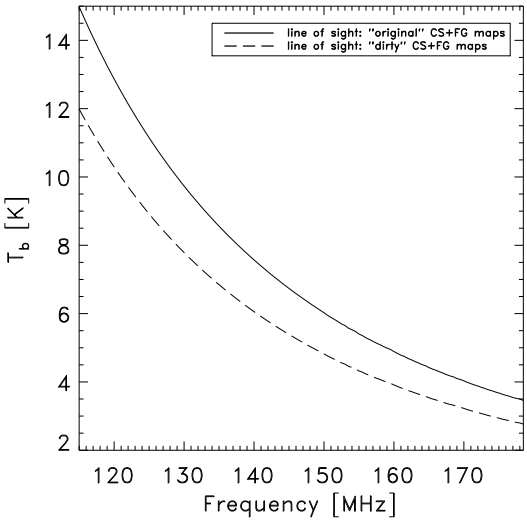

Figure 5.10: One line of sight (one pixel along frequency) of the 'dirty' foreground (FG) + cosmological 21-cm signal (CS) maps (dashed line) in comparison with the same pixel along the frequency of the 'original' FG+CS maps (solid line). The difference between these two lines is due to incomplete uv coverage and its finite extent.

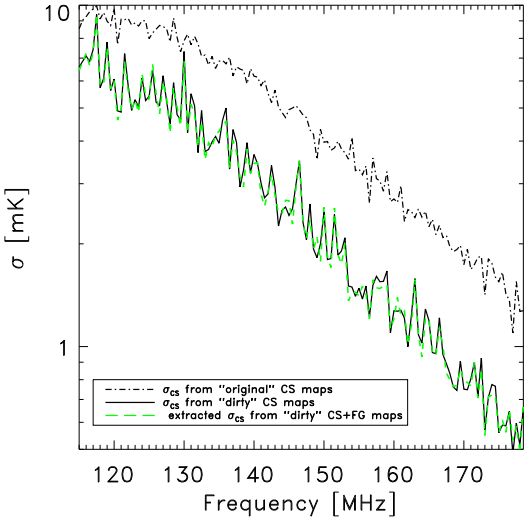

Figure 5.11: Detection of the EoR signal from the simulated simplified 'dirty' foreground maps, without noise, as a standard deviation σ over all lines of sight (dashed green line). The dashed-dotted black line represents the σ over all lines of sight of 'original' EoR signal, while the solid black line the σ over all lines of sight of 'dirty' EoR signal maps.

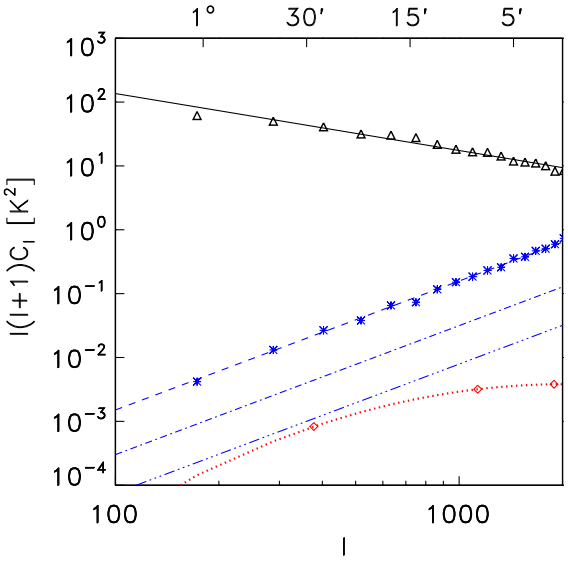

Figure 5.12: Angular power spectra of the simulated EoR signal (dotted red line), simulated dominant component of the foregrounds (solid black line) and three levels of noise: the dashed blue line represents noise for a single beam after one year of integration, the dashed-dotted blue line for five beams after one year of integration and the dashed-dotted-dotted blue line for five beams and four years of integration. The lines are drawn as the best fit to the corresponding points.

Fig. 5.12 shows the angular power spectra of the simulated EoR signal (dotted red line), simulated diffuse component of the foregrounds (solid black line) and three levels of noise (blue lines) at 150 MHz. The lines are drawn as the best fit to the corresponding points. The dashed blue line represents the level of the noise ($\sigma_{\mathrm{noise}}(150\ \mathrm{MHz}) = 52\ \mathrm{mK}$) after one year of the LOFAR-EoR experiment (400 h of total observing time) with a single beam. For this case of instrumental noise and inclusion of realistic diffuse foregrounds we have shown that we are able to statistically detect the EoR signal despite the small signal to noise ratio. However, the current observing plan of the LOFAR-EoR experiment is to observe with five independent beams, which reduces the σ_{noise} by a factor of $\sqrt{5}$ (dashed-dotted blue line). After four years of observations (4×400 h) with five beams the σ_{noise} is reduced by a factor of $\sqrt{20}$ (dashed-dotted-dotted blue line), which means that the signal to noise ratio is roughly 0.5.

5.5 Calibration issues

One of the major challenges of the EoR experiments is the extraction of the EoR signal from the astrophysical foregrounds. The extraction is usually formed in total intensity along the frequency direction due to the following characteristics: the cosmological 21 cm signal is essentially unpolarized and fluctuates along the frequency direction (see

Fig. 5.14), whereas the foregrounds are smooth along the frequency direction in total intensity and should only show fluctuations in polarized intensity (see Fig. 3.5, an example of the Galactic emission that is a dominant foreground component).

All current EoR radio interferometric arrays have an instrumentally polarized response, which needs to be calibrated. If the calibration is imperfect, some part of the polarized signal is transferred into a total intensity and vice versa (hereafter 'leakages'). As a result, the extraction of the EoR signal is more demanding.

Moreover, the polarized signal could have similar frequency fluctuations as the cosmological signal and as such could possibly severely contaminate it. Thus, to reliably detect the cosmological signal it is essential to minimize the 'leakages. We illustrate this thorough an example for the LOFAR telescope, but the problem is common to all current and planned EoR radio arrays.

The 'leakages' of the total and polarized signal are produced by two effects: the geometry of the LOFAR array and the cross-talk between the two dipoles in one LOFAR antenna. The cross-talk, a leakage in the electronics that can cause the power from one dipole to be detected with other, is small compared to the geometric effects and we will ignore it for the purpose of this chapter. However, it will be taken into account in future work (Labropoulos et al, *in preparation*).

The geometry of the LOFAR telescope is such that the array antennae are fixed to the ground. Therefore, the sources are tracked only by beam-forming and not by steering the antennae mechanically towards the desired direction. This implies that, depending on the position of the source on the sky, a non-orthogonal (except in the zenith) projection of the two orthogonal dipoles is visible by the source. This projection further changes as the source is tracked over time. Thus, the observed Stokes brightness of the source, $\mathbf{S_{obs}}$, is given by (Carozzi & Woan, 2009):

$$\mathbf{S}_{obs} = \mathbf{MS}, \tag{5.7}$$

where $\mathbf{M}$ is a Mueller matrix that quantifies the distortions of a true source brightness $\mathbf{S} = (I, Q, U, V)$ based on above geometry-projection effect. The Mueller matrix is defined as:

$$\mathbf{M} = \begin{pmatrix} \frac{1}{2}(1+n^2) & -\frac{m^2}{2} + \frac{(1+m^2)l^2}{2(1-m^2)} & -\frac{lmn}{1-m^2} & 0 \\ \frac{1}{2}(l^2-m^2) & 1 - \frac{m^2}{2} - \frac{(1+m^2)l^2}{2(1-m^2)} & \frac{lmn}{1-m^2} & 0 \\ -lm & -lm & n & 0 \\ 0 & 0 & 0 & n \end{pmatrix} \tag{5.8}$$

with the assumption of a coplanar array. Note that (l, m, n) are direction cosines and that the level of geometry-projection 'leakage' therefore varies across the map.

Figure 5.13 shows calculated leakages for the LOFAR telescope observing at 138 MHz a $5^\circ \times 5^\circ$ patch of the sky around the zenith. For the sky model we use the total and polarized intensity maps of Galactic emission (model B). Further, an instant imaging is assumed, i.e. the sky is not tracked over time. The solid line presents the leakage of total intensity (Stokes I), the polarized signal is presented with the dashed line (Stokes Q) and the dotted line (Stokes U). The leakages are plotted as a function of distance from the center of the image along its diagonal. Note that the leakages are tiny around the center of the image, but they increase towards the edges.

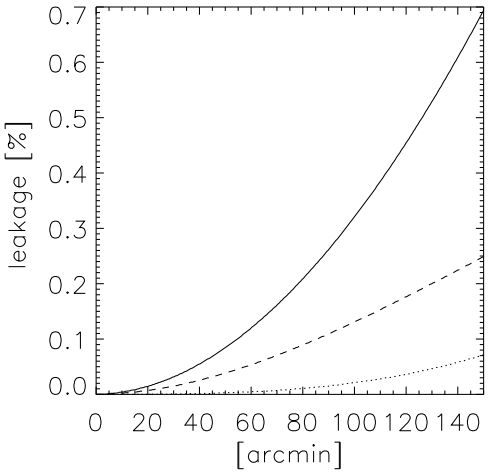

Figure 5.13: Simulated leakages for LOFAR telescope observing at 138 MHz an $5^\circ \times 5^\circ$ patch of the sky around the zenith. The obtained total and polarized intensity maps of Galactic emission (MODEL B) are used as a sky model and an instant imaging is assumed. Solid line presents the leakage of total intensity, and of polarized intensity is presented with dashed line (Stokes Q) and dotted line (Stokes U): see Eq. 5.8. The leakages are plotted as a function of distance from the center of the image along its diagonal.

The same calculation we repeat for an patch of a sky at 45° altitude. The leakages are now much larger, e.g. for the center of the image the leakage to the total intensity is around 2%, but can reach 20% towards the edges of the image. Once the tracking of the sources is taken into account, the calculation becomes even more complex. Detailed results on this issue will be addressed in a forthcoming paper (Labropoulos et al, in preparation).

Here we would like to point out that the 'leakages' caused by the geometry-projection effect are significant. Moreover, if these 'leakages' are not taken properly into account during the calibration of the instrument, the polarized Galactic emission could creep into total intensity signal and severely contaminate the EoR signal (see Fig. 5.14). In other words, the observing window for the EoR experiment should be in regions of the Galaxy that have very low polarized emission and calibration of the instrument should be preformed with such a precession that any remaining residuals of the polarized 'leakages' to the total intensity are much smaller than the EoR signal.

5.6 Summary and Conclusions

Under the assumption of perfect calibration, LOFAR-EoR data maps that include the simulated cosmological 21cm signal ($\sigma_{\rm EoR}(150\ {\rm MHz}) \sim 5$ mK), diffuse components of the foregrounds ($\sigma_{FGs}(150\ {\rm MHz}) \sim 2$ K) and realistic noise ($\sigma_{\rm noise}(150\ {\rm MHz}) \sim 52$ mK) are produced. We refer to this set of parameters as our fiducial model. For noise we assume it has two components, the sky noise and receiver noise. The former varies with frequency

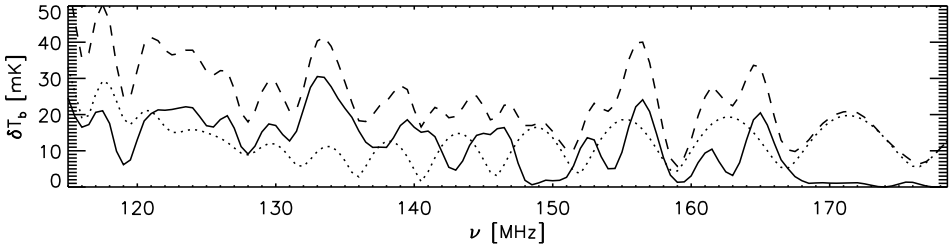

Figure 5.14: A random line of sight through a simulated 21 cm data cube for the 'Stars' patchy reionization history model (*solid line*). *Dotted line* shows the 'leakage' of the polarized Galactic emission to the total intensity and *dashed line* is a sum of the two. We assume 0.15% residual 'leakage' and we use model D as an example of the Galactic emission. The angular and frequency resolution of the data match that of the LOFAR telescope.

as $\nu^{-2.55}$ whereas the latter is roughly frequency independent.

The extraction of the EoR signal is performed along the frequency direction, taking lines of sight (map pixels) one by one. The first step in the EoR extraction is removal of the smooth foregrounds component for each line of sight (see Fig. 5.6). In our analysis we fit a 3^{rd} order polynomial in the logarithmic scale. However, one should be careful in choosing the order of the polynomial to perform the fitting. If the order of the polynomial is too small, the foregrounds will be under-fitted and the EoR signal could be dominated and corrupted by the fitting residuals, while if the order of the polynomial is too big, the EoR signal could be fitted out.

After foreground removal, the residuals are dominated by instrumental noise. Since the noise is unknown for each line of sight and is an order of magnitude larger than the EoR signal, it is an impossible task to directly extract the EoR signal for each line of sight. However, assuming that the statistical properties of the noise ($\sigma_{\rm noise}$) will be known, we can use it to statistically detect the EoR signal. The statistical detection of the EoR signal is the measure of the excess variance over the entire map, $\sigma^2_{\rm EoR}$, that should be obtained by subtracting the variance of the noise, $\sigma^2_{\rm noise}$, from that of the residuals, $\sigma^2_{\rm residuals}$.

Fig. 5.8 shows the results of a successful statistical detection of the EoR signal in the fiducial model of the foregrounds and noise. The detected standard deviation of the signal is in a good agreement with original signal up to 165 MHz. The disagreement for higher frequencies is due to over-fitting caused by the very weak cosmological signal at these frequencies.

In order to see the influence of the foreground and noise level on the EoR extraction and detection, the same analysis was done for models with two and four times bigger foreground levels than in the fiducial model, for a model where the noise is smaller by $\sqrt{2}$, and for a model without noise (see Tabel 5.1). The results are shown in Figs. 5.9 & 5.7.

In the case of higher foreground levels, the EoR signal detection is hampered by over-fitting. In the case of lower noise levels, however, the proposed EoR detection algorithm performs extremely well.

For the diffuse components of simulated foregrounds, a 'dirty' map with realistic but idealised instrumental response of LOFAR is produced (see Fig. 5.4 & 5.5). However, the signal extraction scheme we apply only to the 'dirty' maps that have been produced with

a uniform uv coverage as a function of frequency and have no noise. This is due to the additional difficulties introduced by mixing of angular scales in the frequency direction. Those issues will be discussed in a follow-up paper.

In addition to the signal extraction, we have also demonstrated the need for a good calibration. The importance of this result comes from the fact that the planned EoR radio arrays have a polarized response and the extraction of the EoR signal from the foregrounds is usually performed along the frequency direction. Therefore, if the Galactic foreground is a smooth function (superposition of power laws) along the frequency in a total intensity and it fluctuates in polarized intensity. And the EoR signal is fluctuates along the frequency direction in total intensity, a calibration of the instrumental polarized response can transfer a fraction of the polarized signal into a total intensity. As a result, the leaked polarized emission can mimic the cosmological signal and make its extraction very difficult (see Fig. 5.14).